Opto-Electronic Advances

CN 51-1781/TN ISSN (Print) 2096-4579 ISSN (Online) 2097-3993

Pixel-controlled programmable metasurface as phase-type spatial terahertz modulator

Guibin Li, Guanyi Li, Zehao He*, Xinke Wang, Peter J. Klar*, He Ma* and Yan Zhang*

Citation: Li GB, Li GY, He ZH et al. Pixel-controlled programmable metasurface as phase-type spatial terahertz modulator. *Opto-Electron Adv* **9**, 260028 (2026).

https://doi.org/10.29026/oea.2026.260028

Received: 4 February 2026; Accepted: 9 May 2026; Published online: 3 June 2026

Related articles

Terahertz imaging technology: progress and applications

Yuyuan Tian, Xiaoyin Chen, Zhuocheng Zhang, et al

Opto-Electronic Technology 2026, **2**(1): 250009 doi: 10.29026/oet.2026.250009

Racemic dielectric metasurfaces for arbitrary terahertz polarization rotation and wavefront manipulation

Jie Li, Xueguang Lu, Hui Li, et al

Opto-Electronic Advances 2024, **7**(10): 240075 doi: 10.29026/oea.2024.240075

Generation of structured light beams with polarization variation along arbitrary spatial trajectories using tri-layer metasurfaces

Tong Nan, Huan Zhao, Jinying Guo, et al

Opto-Electronic Science 2024, **3**(5): 230052 doi: 10.29026/oes.2024.230052

Ambient-energy-driven space-time-coding metasurface for space-frequency-division multiplexing wireless communications

Han Wei Tian, Chao Song, Dong Jie Wang, et al

Opto-Electronic Advances 2026, **9**(2): 250229 doi: 10.29026/oea.2026.250229

More related articles in Opto-Electronic Journals Group website

Opto-Electronic Journals Group

https://www.oejournal.org

OE_Journal

@OptoElectronAdv

OEA | Opto-Electronic Advances

Article

September 2026, Vol. 9, No. 9

Open Access

Pixel-controlled programmable metasurface as phase-type spatial terahertz modulator

Guibin Li[1], Guanyi Li[2], Zehao He[1]*, Xinke Wang[1], Peter J. Klar[3]*, He Ma[2]* and Yan Zhang[1]*

Abstract: Reconfigurable intelligent surfaces (RISs) transcend the passive response limitations of conventional metasurface resonators by integrating active materials into metasurface elements, enabling a more flexible control of electromagnetic wave properties. However, RISs devices operating in the terahertz (THz) regime continue to face significant challenges in structural design and multifunctional implementation, particularly regarding optically-addressed THz RISs devices with independent pixel-level encoding, which remain experimentally underexplored. Here, we propose a compact and relatively efficient transmissive programmable metasurface device functioning as a phase-type spatial THz modulator, which enables separate encoding of each pixel within a 50×50 resolution array, thereby achieving dynamic generation and reconfiguration of THz wavefronts. The spatial modulation of the pump pulse intensity locally activates the vanadium dioxide integrated meta-atoms across the metasurface and, thus, defines the specifically designed phase modulation of the cross-polarized transmission. Dynamic wavefront manipulation is then realized by switching the spatial intensity distribution of the pump pulse. Proof-of-concept experiments demonstrate that the same programmable metasurface can perform three distinct functionalities —zoom lens, tunable vortex beam generator, and dynamic hologram. The amplitude conversion efficiency of the device was experimentally measured to be 27%. The programmable scheme demonstrated here paves the way toward miniaturized, integrated, and multifunctional THz optical devices.

Keywords: metasurface; phase change material; programmable; phase-type modulator; pixel-level encoding

DOI: 10.29026/oea.2026.260028 | CSTR: 32247.14.oea.2026.260028

Citation: Li GB, Li GY, He ZH et al. Pixel-controlled programmable metasurface as phase-type spatial terahertz modulator. *Opto-Electron Adv* **9**, 260028 (2026).

1 Introduction

Terahertz (THz) radiation, situated in the electromagnetic (EM) spectrum between infrared and microwave regions, has garnered significant attention and research due to its numerous remarkable properties, including superior penetration capability compared to visible light, distinctive spectral fingerprints, non-ionizing nature, high resolution, high signal-to-noise ratio, as well as unprecedented channel capacity. These exceptional characteristics render THz radiation invaluable for diverse applications encompassing material characterization, communication engineering, homeland security, environmental monitoring, and gas sensing[1–5]. As a promising candidate for signal carriers in six-generation (6G) and future wireless communication systems, the development and innovation of various THz functional devices—including modulators, filters, absorbers, and waveguides—are crucial beyond merely advancing THz sources and detectors[6–11]. Spatial light modulator (SLM) provides precise regulation over amplitude, phase, as well as polarization of EM waves, enabling flexible beam manipulation and serving as an indispensable tool in modern optical systems[12,13]. However, with the increasing requirement of intelligent and multifunctional optical systems, higher requirements have been imposed on THz functional devices to achieve miniaturization, facile integration, and efficient

Received: 4 February 2026

Accepted: 9 May 2026

Published online: 3 June 2026

[1]Department of Physics, Beijing Key Lab for Metamaterials and Devices, Key Laboratory for Terahertz Optoelectronics, Ministry of Education, Beijing Advanced Innovation Center for Imaging Theory and Technology, Capital Normal University, Beijing 100048, China; [2]Institute of Information Photonics Technology, School of Physics and Optoelectronic Engineering, Beijing University of Technology, Beijing 100124, China; [3]Institute of Experimental Physics I, Justus Liebig University, Heinrich-Buff-Ring 16, Giessen 35392, Germany.

*Correspondence: ZH He, E-mail: Hezehao@cnu.edu.cn; PJ Klar, E-mail: peter.j.klar@physik.uni-giessen.de; H Ma, E-mail: mahe_beijing@bjut.edu.cn; Y Zhang, E-mail: yzhang@cnu.edu.cn

control of optical fields[14–16]. Notably, the development of SLM for THz applications remains critically needed, with substantial room for performance enhancement and technological improvement. The rapid advancement of nanophotonics and metasurfaces has provided important solutions to address these challenges.

Metasurfaces, the two-dimensional (2D) metamaterials, are artificially engineered planar devices composed of subwavelength structural elements[17–23]. With the continuous optimization and development of compact integrated systems and demands imposed by complex and dynamic application scenarios, integrating multiple functionalities into a single metasurface has become increasingly imperative. This necessity arises because conventional metasurfaces are passive devices whose primary functions are fixed upon fabrication, which severely constrains their practical applications. Reconfigurable intelligent surfaces (RISs) offer a novel pathway for the design and advancement of devices[24–29]. In the THz regime, the RISs functioning as SLM formed by incorporating tunable materials—such as semiconductors, liquid crystals, phase change materials (PCMs), and graphene—into subwavelength meta-atoms have undergone prominent development in recent years[30–35].

In 2025, Dong et al. proposed a non-interleave heterogeneous integrated structure that exploits the attributes of vanadium dioxide (VO_2), one of the PCMs, to dynamically transform the optical orientation of individual units within a metasurface. Based on the principle of geometric phase, this design enables temperature-dependent thermally manipulated dynamic Pancharatnam–Berry (PB) phase control. However, a significant drawback of the global heating technique is that it can only place the device in two states: before and after heating. To achieve more diverse functionalities, multiple types of metasurface devices need to be fabricated, which impairs their practicality and compactness in actual applications. In the same publication, Dong et al. also fabricated three metasurfaces with different functions to demonstrate switchable anomalous refraction, vortex beam with switchable orbital angular momentum (OAM), and a dynamically tunable holographic display[36]. In 2025, Guo et al. proposed a broadband and transmissive programmable metasurface based on VO_2-metal hybrid structures as an amplitude-type spatial THz modulator (ASTM), comprising 8×8 independently electrically addressable pixels that achieved a modulation depth exceeding 50% across 0.5–1.8 THz range. However, the limited image resolution resulting from the complex electrode configuration, coupled with the functional constraints inherent to pure amplitude modulation, significantly restricts its utility in optical systems[37]. In 2019, Guo et al. proposed a pure phase modulator to generate arbitrary wavefronts of THz beams. By employing femtosecond (fs) pulses with spatial modulation to excite ultra-thin silicon wafers, the desired patterns of metasurface structures are dynamically created. Subsequently, the orientation of subwavelength resonators within the metasurface based on PB phase is dynamically reconstructed by altering the spatial intensity distributions of fs pulses, thereby modulating the wavefront of THz beams. Two proof-of-concept applications were experimentally demonstrated: streaming holographic images and lenses with variable focal length. However, the extremely fragile structural integrity resulting from the 10-μm thick wafer in conjunction with a conversion efficiency of only less than 4%, poses substantial challenges for both device integration and operation[38] (See more discussion and comparison with related works in Supplementary Section 1). With the aim of overcoming the prevailing design and development bottlenecks of THz SLMs, there is a pressing need for multifunctional metasurface platforms operating in the THz regime that offer efficient and independent pixel-level programmability and enable a full 2π phase tuning range for each pixel. Two principal strategies have been pursued to realize such pixel-level programmability: optical addressing and electrical addressing. Electrically addressed programmable metasurfaces inherently encounter considerable limitations, including high fabrication complexity, sophisticated electrode routing, and substantial spatial footprint of the electrodes, which collectively restrict the number of effectively controllable pixels and ultimately impede device scaling and progression. In contrast, optically addressed programmable metasurfaces circumvent these constraints and exhibit unique advantages such as enhanced fabrication feasibility, high-density integration of optical functionalities, and a significantly increased capacity for independently addressable pixels.

In recent years, significant breakthroughs in the patterned fabrication of the VO_2 film have opened up promising avenues for developing high-performance reconfigurable THz metasurface devices. Here, we present a compact, easily integrable, and efficiently transmissive optically-addressed programmable metasurface as a phase-type spatial THz modulator (PSTM) based on VO_2. This device concept enables pixel-level encoding and flexible manipulation of THz wavefronts through patterned pulsed optical excitation. The meta-atoms of the programmable metasurface device consist of metallic split-ring resonators (SRRs) where four structured VO_2 patches are embedded into the gaps. Depending on the intensity of the pump beam on a patch, a specific phase change of the corresponding segment of the SRR can be selected by utilizing the reversible insulator-metal-transition (IMT) of VO_2 at this patch. By illuminating a meta-atom by a spatial pump-beam intensity-distribution, all four segments of the SRR can be addressed independently. Controlled variation of the spatial pump-beam intensity-distribution on the SRR allows us to realize a four-value discretized linear phase gradient of defined phase-shift values within the range of 0 to 2π for the transmissive cross-polarized component of the meta-atom at a working frequency of 0.7 THz. Subsequently, we arrange the meta-atoms integrated with VO_2 in a periodic array and activate the entire metasurface with patterned pump pulses gener-

ated according to the phase encoding sequence required for the meta-atoms of the array for achieving the desired functionality. The proof-of-concept experiments demonstrate the possibility of arbitrarily switching between different functionalities —including zoom meta-lens with alterable focal lengths, tunable focused vortex beams, and dynamic holographic imaging —simply by transforming the spatial intensity distribution of the pulsed pump-beam. The proposed device offers significant advantages in terms of flexibility, stability, and powerful functionality, providing valuable design strategies for enhancing THz wireless communications and high-resolution imaging.

2 Results

2.1 Concept design

A vivid and concrete conceptual demonstration of dynamic holographic imaging realized through a pixel-controlled programmable metasurface functioning as a PSTM is presented in Fig. 1. The key to successful implementation lies in constructing meta-atoms that simultaneously possess full 2π phase modulation coverage and reconfigurability. Here, we employ metallic structures based on C-shaped split-ring resonators (CSRRs), which are crucial for achieving efficient linear polarization conversion with specific phase delays. Furthermore, to enable device reconfigurability, we optimize and modify the structure of CSRRs. A 200 nm-thick VO_2 thin film fabricated on a polyimide (PI) flexible substrate is patterned and precisely embedded into the CSRRs, ultimately forming VO_2-based C-shaped split-ring resonators (V-CSRRs) structure. Utilizing the reversible IMT of VO_2, the V-CSRRs can dynamically and effectively manipulate THz wavefronts on demand while maintaining reconfigurability. The designed meta-atoms are arranged periodically in a chessboard-like array to form the final metasurface device.

The femtosecond laser pulse is modulated by an optical mask to form an illumination pattern, i.e., spatial intensity distribution, corresponding to the desired spatial phase distribution on the metasurface. The patterned pump beam passes through a 4f imaging system (not shown) to improve image quality before being projected onto the device. The VO_2 patches located within the four gaps of the V-CSRRs hit by the intense pulse beam undergo local thermal heating inducing spatially selective the IMT in those VO_2 patches. Upon illumination by an *x*-polarized THz beam, the metasurface enables precise manipulation of the transmitted cross-polarized component through tailored phase modulation, facilitating subwavelength-scale wavefront engineering to realize prescribed field configurations for dynamic holographic imaging and other versatile functionalities.

The V-CSRR meta-atom structure is illustrated in Fig. 2(a). It comprises a gold CSRR layer and strategically embedded VO_2 patches integrated on a flexible PI substrate. The meta-atom harnesses photothermal accumulation arising from light–matter interactions. Upon selective

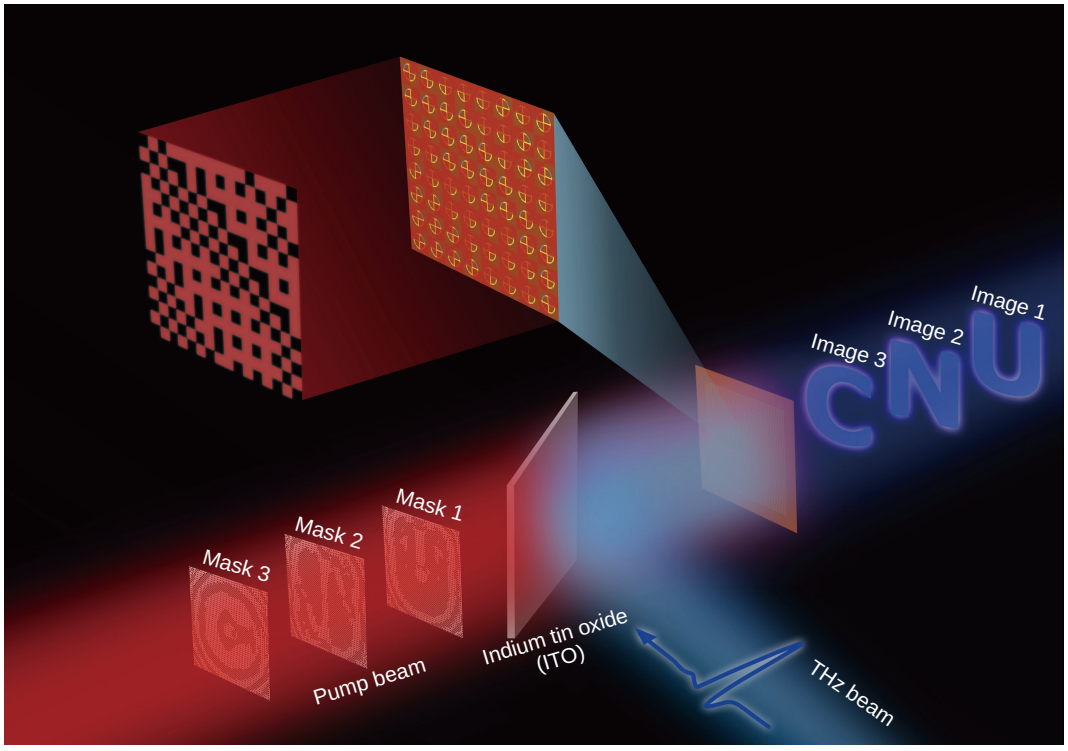

Fig. 1 | Schematic of the pixel-controlled programmable metasurface as a PSTM.

illumination of the VO_2 patches with an intense pulsed beam, localized heating triggers a complete IMT transition. A central requirement for realizing optically addressed, pixel-level programmability is to confine the photothermally generated heat within the VO_2 patches while suppressing thermal dissipation. This renders substrate selection a critical design factor. Compared with conventional VO_2 supporting substrates such as sapphire, the PI substrate is favored as its low thermal conductivity and outstanding structural stability.

Figure 2(b, c) present the simulated steady-state temperature distributions of the V-CSRR meta-atom on sapphire and PI substrates, respectively, under spatially selective photoexcitation corresponding to coding state M_2, with a 65 °C thermal offset applied at the substrate bottom. Owing to its high thermal conductivity, sapphire prevents heat localization within the VO_2 patches, while the PI substrate efficiently confines the photo-induced thermal energy and suppresses thermal crosstalk. This fundamentally addresses the heat dissipation challenge and provides the necessary thermal isolation for enabling reliable optically addressed programmability (see Supplementary Section 2 for details).

An optical photo of the fabricated programmable metasurface is demonstrated in Fig. 2(d), featuring a 50 × 50 pixel array. The upper inset presents a microscopic view of a representative region, confirming the successful realization of the designed programmable THz metasurface (see Methods for fabrication procedures). The four rectangular structures surrounding the pixel array play a crucial role in enabling precise pixel-level alignment between the patterned pump pulses and the meta-atoms within the metasurface (see more details in 4.2 THz imaging measurement).

The phase shift induced by a meta-atom depends on the state (insulating or metallic) of the four VO_2 patches of the V-CSRR. If an *x*-polarized THz beam is normally incident on a meta-atom and all VO_2 patches are in the insulating state, the phase shift induced by the meta-atom is near zero. Thus, no cross-polarized transmitted electric field component occurs, i.e., the polarization conversion capability is zero. However, by applying a spatially selective optical excitation to the VO_2 patches within the V-CSRRs and the IMT effect is triggered in one or more VO_2 patches within the V-CSRRs, a specific non-zero phase shift can be adjusted. Adjusting the phase shift of all meta-atoms on the

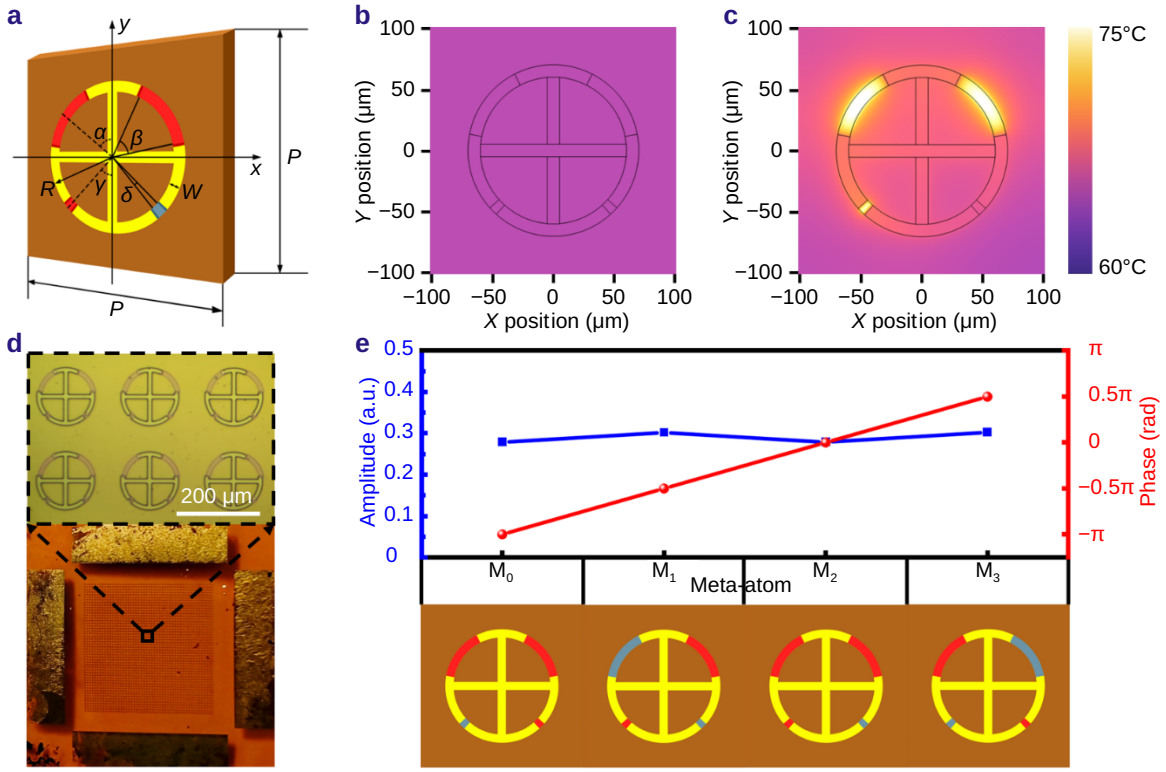

Fig. 2 | Design of the meta-atom in the programmable metasurface. (a) Schematic diagram of the V-CSRRs unit (meta-atom) with one gap containing a VO_2 patch at -45° in its insulating (gray) state and other gaps with VO_2 patches in their metallic (red) state. (b, c) Simulated thermal distributions for the meta-atom located on the Sapphire (b) and PI (c) substrate, respectively. (d) Optical photo of the successfully fabricated programmable metasurface. The inset displays a microscopic image of the sample, where the scale bar represents 200 μm. (e) Simulated cross-polarized transmission amplitude and phase responses of the proposed meta-atoms for four distinct coding states under normal incidence of an *x*-polarized THz wave at 0.7 THz. The insets illustrate the selective IMT configurations of the VO_2 patches for coding states M_0–M_3. Adjacent coding states yield nearly identical amplitude while introducing a phase increment of approximately π/2.

metasurface in this way yields a precise control over both amplitude and phase, of the re-emitted cross-polarized THz field. The complete structural parameters of the meta-atom are presented in Fig. 2(a). The unit cell period P is 200 μm. The PI substrate has a thickness of 100 μm. Both the VO_2 patches and the gold thin layer have a thickness of 200 nm. The outer radius R of the C-shaped ring is 69 μm, with a linewidth W of 10 μm. The azimuthal angles α and γ, defined as the angles between the gap symmetry axis and the y-axis, are 53° and 45°, respectively. The gap opening angles β and δ are 52° and 6°, respectively. It is noteworthy that the split gaps of the C-shaped rings are designed to be symmetric about the y-axis, enabling precise introduction of a π phase retardation in the cross-polarized transmission phase modulation.

We implemented 2-bit encoding for the reconfigurable and programmable meta-atoms to create four distinct coding states (M_0, M_1, M_2, and M_3), designed to modulate the phase of the cross-polarized electric field component across the range from 0 to 2π while achieving equal amplitude at 0.7 THz. Full-wave electromagnetic simulations were executed via the finite-difference time-domain approach implemented in commercial FDTD Solutions. The simulation model was constructed based on the structure and geometric parameters shown in Fig. 2(a). Periodic boundary conditions were conducted in both x and y directions, while perfect matching layers were employed as the boundary conditions in the transmission direction. Key material parameters were set according to prior experimental characterization: The refractive index of PI was set to 1.75, and the conductivities of VO_2 patches were set to 5×10^2 S/m and 1×10^5 S/m, corresponding to the insulating and metallic states, respectively. Additionally, the gold layer was modeled as a perfect electrical conductor. The simulated amplitude and phase responses of the cross-polarized transmitted field at 0.7 THz for the meta-atoms in the four coding states are presented in Fig. 2(e). The insets show details of the specific configurations of selected IMT state of the four VO_2 patches in each coding state, where the color 'gray' represents the insulating state and 'red' the metallic state. The simulation results indicate that the four coding states successfully achieve phase regulation of the transmitted cross-polarized THz waves over a 2π range at 0.7 THz, maintaining a fixed phase interval of π/2 while preserving the simulated cross-polarized transmission amplitude of approximately 30%. The amplitude conversion efficiency (ACE) is now defined as:

$$ACE = \left| \frac{E_y^{\text{out}}}{E_x^{\text{in}}} \right| , \tag{1}$$

where E_x^{in} represents the complex amplitude of the normally incident x-polarized THz wave, and E_y^{out} denotes the complex amplitude of the transmitted cross-polarized (y-polarized) field component. This formula characterizes the efficiency of polarization conversion at the system level. In this definition, ACE quantifies the efficiency of polarization conversion from the incident x-polarized field to the transmitted y-polarized field. Based on this definition, when all VO_2 patches in the V-CSRR structure are in the insulating state, the meta-atom does not support polarization conversion, resulting in a negligible cross-polarized component E_y^{out} and, consequently, an amplitude conversion efficiency close to zero. In contrast, when the meta-atom operates in one of the four coding states (M_0–M_3), polarization conversion is enabled, leading to a finite cross-polarized component and a nonzero ACE.

Experimentally, the ACE is obtained as follows. First, the metasurface is illuminated by a normally incident x-polarized THz wave, and the transmitted cross-polarized field at 0.7 THz is measured using the optical-pump THz-imaging system. The field amplitude is integrated over the spatial region corresponding to the metasurface to obtain the numerator. Then, the sample is removed, and the co-polarized transmitted field under identical conditions is measured and integrated over the same region to serve as the reference (denominator). The ratio of these two quantities yields the experimentally measured ACE, which is approximately 27%. We further note that this experimentally measured value is slightly lower than the simulated cross-polarized transmission amplitude of an individual meta-atom (Fig. 2(e)). This difference is expected, as the overall efficiency of the metasurface is influenced by additional factors, including illumination non-uniformity, finite aperture effects, and inter-element coupling. Therefore, the unit-cell transmission efficiency and the system-level conversion efficiency are fundamentally different quantities.

Moreover, the limited transmission amplitude is primarily attributed to the relatively low polarization conversion efficiency of monolayer metallic metasurfaces, which is further affected by the incorporation of PCMs. Nevertheless, our design still exhibits satisfactory polarization conversion performance. Notably, due to the limited intensity of femtosecond laser pulses in optical-pump THz-imaging system (see details in Methods), optical excitation alone is insufficient to induce the phase change in VO_2 patches. Our strategy involves first applying a thermal offset of 65 °C to the metasurface sample to bring the VO_2 near its phase transition temperature, followed by illumination with a pump laser beam at a power density of 800 mW/cm^2, which triggers complete IMT in VO_2 through thermal accumulation effect. Additionally, before conducting the proof-of-concept experiments, device performance characterization was implemented on the fabricated metasurface samples to ensure proper functionality (see details in Supplementary Section 3, 4, 5).

2.2 Dynamic zoom meta-lens

To present the flexibility and versatility of the proposed programmable metasurface as a PSTM, we first design and

experimentally validate a dynamic zoom meta-lens. Compared to a monofocal meta-lens, a zoom meta-lens exhibits multifocal capabilities. Thus, it has significant advantages in flexibility, compact design, and efficient tunability and demonstrates considerable potential for advanced optical applications[39–43]. By engineering the phase distribution of the metasurface, the THz radiation scattered by meta-atom arrangement can constructively interfere to a high intensity spot in the focal plane, analogous to the wavefront manipulation in a conventional lens. According to geometric optics, the design of a meta-lens requires that the phase shift $\varphi(x, y)$ imparted at each position on the metasurface satisfies:

$$\varphi(x,y) = -\frac{2\pi}{\lambda}\left(\sqrt{x^2+y^2+f^2}-f\right), \tag{2}$$

where λ denotes the operating wavelength, (x, y) represent the spatial coordinates on the metasurface, and f is the designed focal length.

Here, we selected f_1 = 10 mm and f_2 = 12 mm as the two reconfigurable focal lengths to validate the dynamic focusing performance of the meta-lens. At the operating frequency of 0.7 THz, we calculated the spatial phase profile distributions for both chosen focal lengths, performed a four-value phase discretization and encoding operations according to the results shown in Fig. 2(e), ultimately generating the mask patterns required for the experiments (see detailed configurations in Supplementary Section 6). We employed the optical-pump THz-imaging system to experimentally characterize the programmable metasurface lens. In this system, the 800 nm pulsed beam possessed an optical power density of approximately 800 mW/cm^2, with a spot diameter of approximately 16 mm, providing sufficient coverage of the mask patterns. Figure 3(a, b) presents the THz intensity distributions of the y-polarized electric field component in the yz plane after transmission of x-polarized THz radiation falling at normal incidence on the metasurface (with normal vector along the z-direction) for the two meta-lens configurations with focal lengths f_1 = 10 mm and f_2 = 12 mm. The same value ranges along the y and z directions in both graphs facilitate direct comparison of the results. As shown, at 0.7 THz, the designed programmable metasurface demonstrates excellent focusing performance for THz beams at both reconfigurable focal lengths, with the

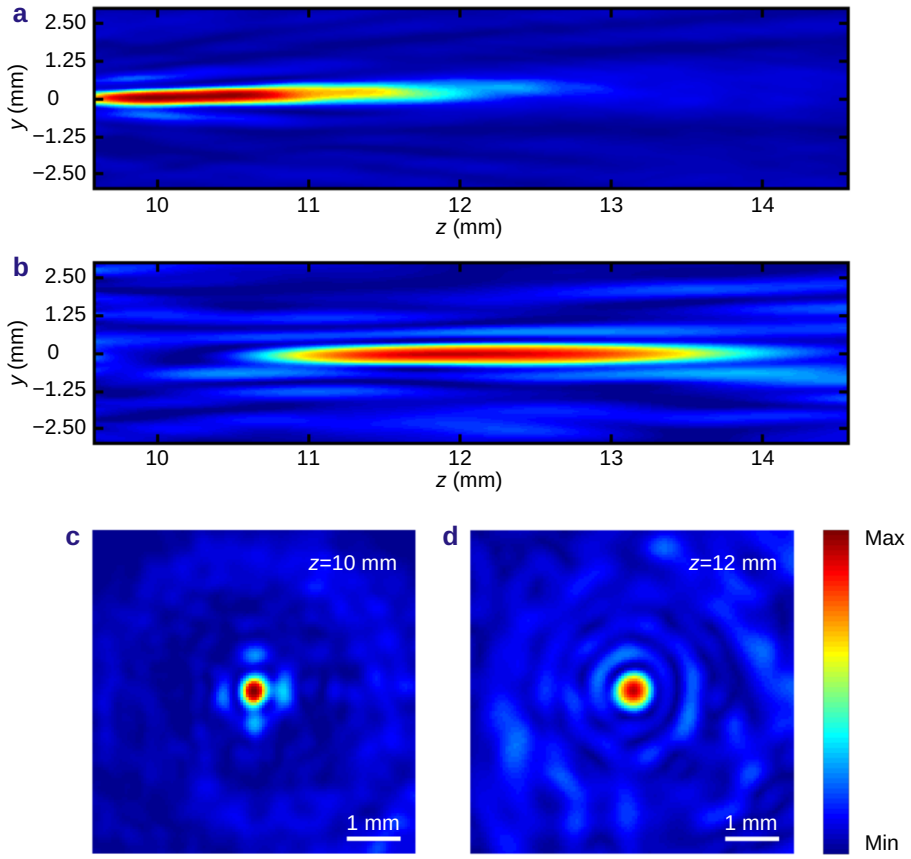

Fig. 3 | Experimental demonstration of the THz dynamic zoom meta-lens. (a, b) Experimental results of y-polarized THz electric field profile in the yz plane, when the metasurface (surface normal vector along z-direction) is illuminated with x-polarized THz waves, for the designed zoom meta-lens with focal lengths f_1 = 10 mm (a) and f_2 = 12 mm (b), respectively. (c, d) Measured results of the THz electric field intensity, extracted at the corresponding focal planes from (a) and (b), respectively.

experimentally observed focal plane positions revealing results highly consistent with the designed values. To further characterize the focusing capability of the meta-lens in the two configurations, the measured THz intensity distributions in the respective focal planes (*xy* planes at z =10 mm and 12 mm) are shown in Fig. 3(c, d). Analysis of the imaging results clearly reveals that both reconfigurable focal spots exhibit well-defined circular profiles, with nearly all intensity concentrated at the focal points. The experimentally measured amplitude conversion efficiency was calculated to be 27%. The successful design and experimental presentation of the programmable metasurface as a THz dynamic zoom meta-lens validates the device's flexibility and its potential for practical applications.

2.3 Focused vortex beam with tunable topological charges

In the following, we discuss a focused vortex beam generator. From the quantum mechanical perspective, the OAM carried by photons is associated with the “twist” of helical phase front of the form $\exp(il\psi)$, where ψ denotes the azimuthal angle and l represents the mode number[44–47]. To create a focused vortex beam, it is necessary to integrate two diverse features —focusing and spiral phase modulation — into a single metasurface[48–53]. Accordingly, the total phase distribution $\phi(x, y)$ at any position on the metasurface can be expressed as:

$$\phi(x,y) = -\frac{2\pi}{\lambda}\left(\sqrt{x^2+y^2+f^2}-f\right) + l\cdot\arctan\left(\frac{y}{x}\right), l = \pm 1 , \tag{3}$$

where λ is the operating wavelength, (x, y) denote the spatial coordinates, f represents the predefined focal length, and l is the topological charge. According to this equation, we can calculate the spatial phase distribution across the metasurface and perform encoding to obtain the corresponding pump mask patterns with a four-value discretized phase (see details in Supplementary Section 7).

Figure 4(a, b) illustrate the simulated spatial distributions of THz field intensity and phase on the focal plane (equivalent to focal length of f = 11 mm) for the focused vortex beam generator operating at 0.7 THz, corresponding to topological charges of l = +1 and l = −1, respectively. The aforementioned optical-pump THz-imaging system was employed to experimentally characterize the focused vortex beams. The x-polarized THz beam propagating along the z-direction was normally incident on the programmable THz metasurface, and the y-polarized radiation component was detected. The experimentally measured intensity and phase distribution on the focal plane (z = 11 mm) are presented in Fig. 4(c, d) for both topological charges of l = +1 and l = −1, which can be dynamically tuned by switching the pump mask patterns. The simulation and experimental results exhibit very good agreement, both clearly displaying well-defined annular intensity distributions with a hollow center, resembling a "donut" shape. Correspondingly, the helical phase distributions rotating counterclockwise or clockwise are observed in the central region, characterized by a phase singularity located at the center and undergoing a complete 2π phase variation along the closed loop. These results are consistent with the characteristic behavior of +1st-order and −1st-order focused vortex beams.

To visualize the phase variation more intuitively, we extracted the phase data from the imaging results at different azimuthal angles for both l = +1 and l = −1 focused vortex beams at a fixed radial distance of r = 0.8 mm, as plotted in Fig. 4(e, f), respectively. Both curves demonstrate an excellent linear relationship between phase and azimuthal angle. Furthermore, to quantitatively evaluate the mode purity of the focused vortex beams, we calculated the correlation coefficients combining the simulation and experimental results, as illustrated in Fig. 4(g). Specifically, the correlation coefficient is defined as:

$$C = \left|\iint E_{\mathrm{v}}(E_{\mathrm{s}})^{*} r\mathrm{d}r\mathrm{d}\psi\right|^{2} , \tag{4}$$

where E_{v} and E_{s} denote the normalized complex field amplitudes of the experimentally measured and simulated THz vortex beams, respectively; the asterisk (*) represents complex conjugation, and (r, ψ) are the polar coordinates. Both fields are normalized prior to calculation to ensure a fair comparison. This definition clarifies the origin of the reported correlation coefficients. The correlation coefficients for both, l = +1 and l = −1, exceed 80%, demonstrating high mode purity[54]. These results collectively confirm that the designed programmable metasurface as a PSTM can successfully generate THz focused vortex beams with tunable topological charge in experimental implementation.

2.4 Dynamic holographic imaging

In the final demonstration, the designed metasurface device is employed for dynamic holographic imaging[55–58]. Specifically, we calculated the spatial phase profiles required for THz dynamic holographic imaging according to the Gerchberg-Saxton (GS) algorithm. The letters “C”, “N” and “U” were used as target images. By an iterative optimization process, three phase holograms of the THz metasurface based on the four discrete phase values of the meta-atoms were ultimately obtained. The corresponding simulated reconstruction results are demonstrated in Fig. 5(a–c). Subsequently, the discrete phase values in the holograms were encoded and corresponding masks were generated to enable patterned manipulation of the pump pulses in the experiments (see detailed configurations in Supplementary Section 8). The experimental characterization was performed using the identical optical-pump THz-imaging system described above, leaving all system configurations unchanged except for the mask patterns. According to the

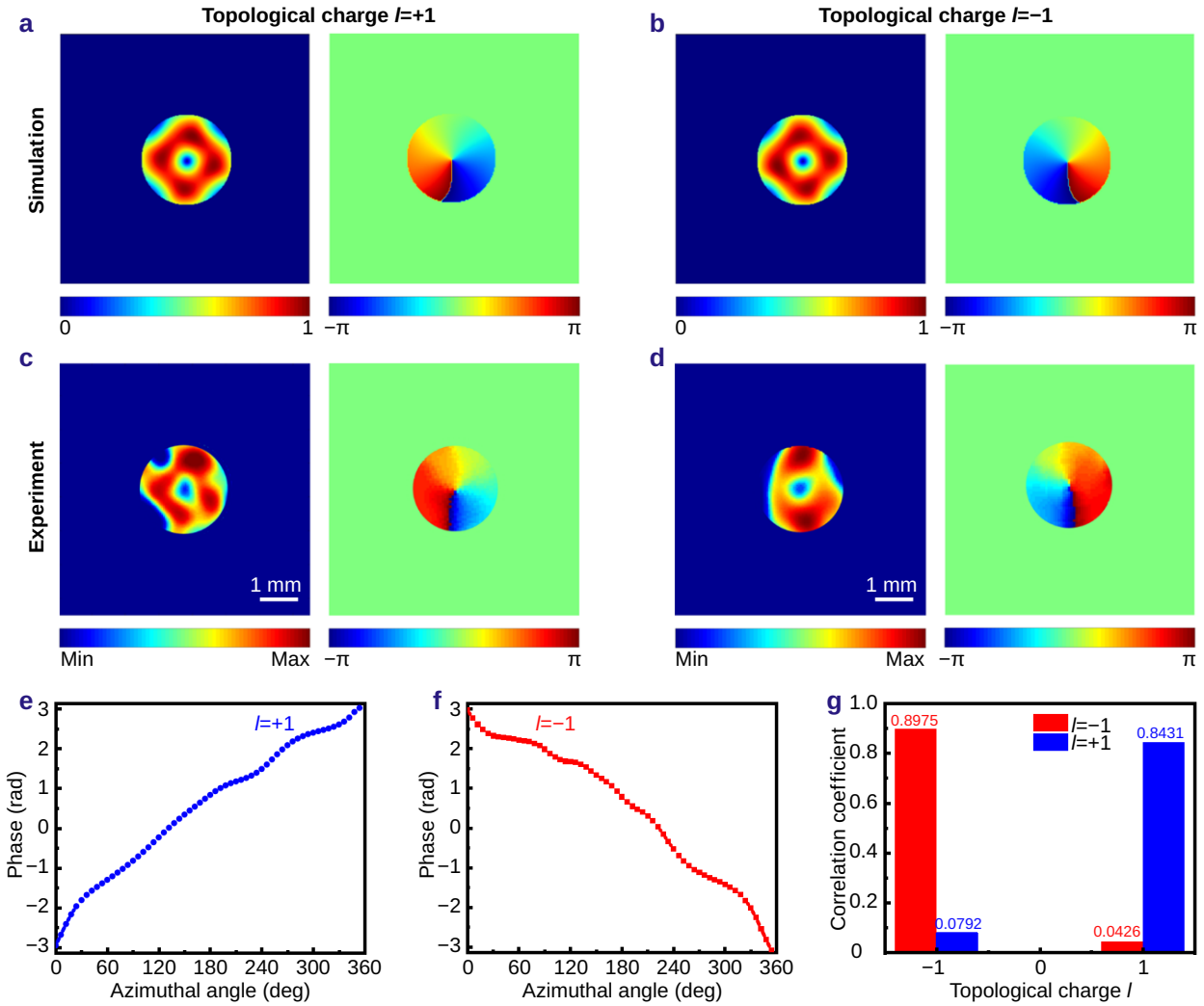

Fig. 4 | Generation of focused vortex beam with tunable topological charges. (a, b) Simulated normalized THz field intensity and phase distributions for topological charges l = +1 and l = −1. (c, d) Intensity and phase distributions of the focused THz vortex beams at focal plane (z = 11 mm) for the design frequency of 0.7 THz experimentally measured by optical-pump THz-imaging system for topological charges l = +1 and l = −1. The scale bar is 1 mm. (e, f) Relationship between phase variation curves and azimuthal angle for l = +1 and l = −1 with the radial distance r = 0.8 mm. (g) Correlation coefficients of the experimentally measured focused vortex beams with different topological charges.

hologram design, for an x-polarized incident THz beam, the complex amplitude information of the transmitted y-polarized electric field was collected in the observation plane located 12 mm behind the sample. The experimentally measured intensity distributions for the three letters obtained at the operating frequency of 0.7 THz are shown in Fig. 5(d–f). The images clearly demonstrate that the reconstruction of the letters “C”, “N” and “U” is feasible and that dynamic switching between different letters is possible by dynamically changing the mask patterns. We introduce a quantitative fidelity metric to evaluate the agreement between reconstructed and target field distributions. The fidelity is defined as[59]:

$$F = \left| E_{\text{measured}} E^{*}_{\text{target}} \right|^{2}, \tag{5}$$

where E_{measured} and E_{target} represent the normalized measured and target complex field distributions, respectively. Based on this metric, the fidelities of the reconstructed letters “C”, “N”, and “U” are 0.8126, 0.7671, and 0.7037, respectively. The experimental results demonstrate good agreement with the Gerchberg–Saxton (GS) design targets successfully verifying the flexibility and effectiveness of the proposed programmable metasurface as a PSTM for dynamic holographic imaging. The imperfections in the reconstructed images, both theoretically and experimentally, are primarily attributed to the limited number of metasurface units (50×50) and the discrete phase quantization with 2-bit resolution only. Additionally, since the device was fabricated on a flexible substrate, minor alignment errors may occur during pixel-level alignment between the patterned pump

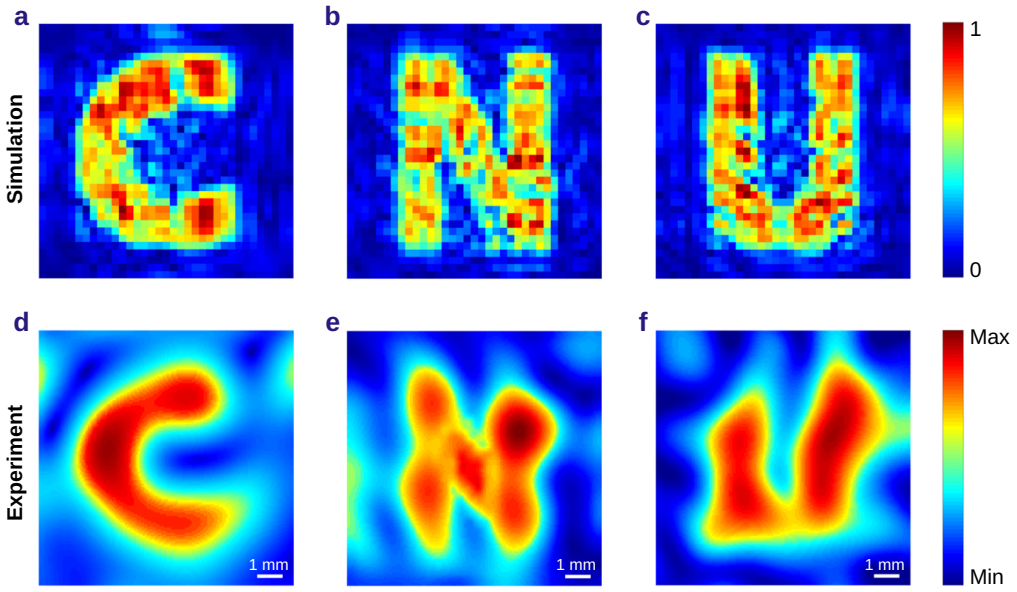

Fig. 5 | Experimental results of dynamic holographic imaging. (a–c) Theoretical expectations of letters “C”, “N” and “U” reconstructed by the GS algorithm, respectively. (d–f) Experimental results for measured holographic images of the letters “C”, “N” and “U” at 0.7 THz, respectively. The scale bar is 1 mm.

pulses and the meta-atoms and may affect the reconstruction results. The results show that the device performance remains stable for misalignments within 15 μm, with no significant degradation observed in the reconstructed field distributions. This confirms that the system exhibits good tolerance to the minor alignment errors.

3 Discussion

The proposed programmable metasurface, functioning as a 2-bit phase-type efficiently transmissive spatial THz modulator, features a large number of programmable pixels and demonstrates an advanced design paradigm with robust capabilities for optically-addressed pixel-level separate encoding. This enables flexible manipulation and reconfiguration of THz wavefronts, holding significant implications for the advancement of nanophotonics and the development of metasurface devices. Nevertheless, the proposed approach still provides room for further optimization and enhancement. First, as a spatial THz modulator, the performance of the designed programmable metasurface is determined by its response speed and maximum refresh rate to a certain extent. In the present characterization, the relatively limited temporal response—characterized by a rise time of 562 ms and a fall time of 406 ms—and the low refresh rate (~1 Hz) are primarily constrained by the mechanism used to trigger the IMT of the VO_2 patches within the meta-atoms, namely the photo-induced thermal accumulation effect. Alternatively, employing a semiconductor-based optical excitation scheme to generate photocarriers could significantly enhance the transient response and enable high-speed modulation of THz fields.

Second, there remains space for improving the device efficiency. It is well established that the amplitude conversion efficiency of single-layer metallic metasurfaces is fundamentally limited to 50%, while the incorporation of VO_2 phase-change materials further reduces this efficiency. Nevertheless, the experimentally demonstrated amplitude conversion efficiency in the present proof-of-concept reaches 27%, indicating reasonably good performance. Future improvements may be achieved by adopting design strategies such as double-layer metallic metasurfaces or integrating metallic grating structures on the opposite side of the substrate, thereby enhancing overall device efficiency.

Finally, in the dynamic modulation of THz wavefronts using the proposed programmable metasurface, switching between different optical functionalities currently requires replacing the corresponding optical mask, which inevitably increases operational complexity. At an early stage of this work, we attempted to employ a digital micromirror device (DMD) to dynamically modulate the spatial intensity distribution of the pulsed pump beam used to trigger the IMT in the VO_2 patches. However, the high peak power density of the pump pulses exceeded the damage threshold of the DMD, resulting in irreversible device failure. In future implementations, DMDs or other spatial light modulators with higher damage thresholds could be employed to achieve dynamic beam shaping, thereby eliminating the need for physical mask replacement and significantly simplifying the operation. Despite this current limitation, the proposed programmable metasurface demonstrates robust capability for optically addressed, pixel-level independent

encoding, enabling dynamic generation and reconfigurable manipulation of THz wavefronts. This work also provides valuable guidance for optimizing device design and improving operational performance in future applications.

In conclusion, we have presented an efficient programmable metasurface as a PSTM that exploits the reversible IMT of VO_2 to enable flexible THz wavefront manipulation. We fabricated the designed metasurface device and performed proof-of-concept experiments, including a zoom meta-lens, a focused vortex beam with tunable topological charges, and dynamic holographic imaging. Dynamic switching between these functionalities was effectuated by modulating the patterns of pump-pulse beam, showcasing the remarkable potential of the proposed programmable THz metasurface in terms of versatility and flexibility. The metasurface device demonstrated here establishes a foundation for the design and innovation of reconfigurable and programmable metasurface based on tunable materials, offering promising prospects for next-generation wireless communication systems.

4 Materials and methods

4.1 Device fabrication

The fabrication was conducted as follows: First, a commercially purchased 100 μm-thick PI film was sequentially cleaned in acetone, absolute alcohol, and deionized water, followed by drying in a nitrogen flow to ensure a contamination-free surface. The PI film was then tightly fixed on a 1 mm-thick quartz substrate to facilitate subsequent processing. Next, a 200 nm-thick VO_2 film was deposited on a separate precleaned quartz substrate and subsequently transferred onto the PI film (see more details in Supplementary Section 9). Periodic patterned VO_2 patches were formed using standard ultraviolet photolithography and reactive ion etching. Then, the complementary patterns of the metallic structures were formed by standard ultraviolet photolithographic techniques. Finally, 10 nm-thick titanium and 200 nm-thick gold films were deposited by magnetron sputtering. After the lift-off process, the sample fabrication was complete (see more details in Supplementary Section 10). The finished samples were carefully peeled from the quartz substrate for subsequent experimental characterization.

4.2 THz imaging measurement

For experimental validation, a home built optical-pump THz-imaging system was employed to conduct proof-of-concept demonstrations of the designed programmable THz metasurface. Ultrashort pulses emitted from a Ti: sapphire regenerative amplifier (800 nm central wavelength, 1 kHz repetitive rate, 100 fs pulse duration) were divided into three paths: pump, THz generation, and THz detection. The pump path was employed to project encoded mask patterns—configured according to the desired optical functionality —onto the metasurface sample. A 4f imaging system comprising two identical biconvex lenses was incorporated into the projection pathway to enhance image quality. Spatial alignment between the projected mask patterns and the metasurface sample was achieved with pixel-level precision by utilizing an industrial CMOS camera equipped with a matching objective lens, enabling unit-cell-level control of the metasurface.

Specifically, the spatial alignment process is implemented in two stages: coarse alignment and fine alignment. During the coarse alignment stage, the four rectangular markers surrounding the metasurface pixel array (Fig. 2(d)) are utilized. Based on their geometric positions, four corresponding rectangular features are incorporated into each optical mask during fabrication. As a result, the patterned pump beam also contains these reference features after modulation. Coarse alignment is achieved by spatially matching these features with the corresponding markers on the metasurface, ensuring global registration. Since coarse alignment alone is insufficient for precise operation, a fine alignment stage is subsequently performed. This step is implemented using an industrial CMOS camera equipped with a matched objective lens, enabling pixel-level spatial registration between the optical pattern and the metasurface.

The THz generation beam was irradiated on a ZnTe crystal to generate x-polarized THz radiation, which was subsequently redirected by an indium tin oxide (ITO) film and delivered at normal incidence to the metasurface sample. The ITO film is employed as a dichroic mirror that allows efficient transmission of the optical pump beam and efficient of reflection of THz beam. The transmissive THz wave was probed via a second ZnTe crystal. The probe beam was utilized for retrieve the complex amplitude of the THz electric field. By precisely controlling the temporal delay between the THz and detection paths using an electric translation stage, the THz time-domain spectra were acquired. At each position of delay time, 64 frames were captured by the CCD camera and averaged to enhance the signal-to-noise ratio. Frequency-resolved THz images were subsequently obtained via Fourier transformation. Furthermore, the detected polarization component of the THz electric field could be adjusted by switching the polarization state of the probe beam (see more details in Supplementary Section 11).

References

1. Tonouchi M. Cutting-edge terahertz technology. *Nat Photonics* **1**, 97–105 (2007).
2. Ferguson B, Zhang XC. Materials for terahertz science and technology. *Nat Mater* **1**, 26–33 (2002).
3. Nagatsuma T, Ducournau G, Renaud CC. Advances in terahertz communications accelerated by photonics. *Nat Photonics* **10**, 371–379 (2016).
4. Sun QS, Chen XQ, Liu XD et al. Exploiting total internal reflection geometry for terahertz devices and enhanced sample characterization.

Adv Opt Mater **8**, 1900535 (2020).
5. Siegel PH. Terahertz technology. *IEEE Trans Microw Theory Tech* **50**, 910–928 (2002).
6. Gu JQ, Singh R, Liu XJ et al. Active control of electromagnetically induced transparency analogue in terahertz metamaterials. *Nat Commun* **3**, 1151 (2012).
7. Chen HT, Padilla WJ, Cich MJ et al. A metamaterial solid-state terahertz phase modulator. *Nat Photonics* **3**, 148–151 (2009).
8. Zheludev NI, Kivshar YS. From metamaterials to metadevices. *Nat Mater* **11**, 917–924 (2012).
9. Tao H, Bingham CM, Strikwerda AC et al. Highly flexible wide angle of incidence terahertz metamaterial absorber: design, fabrication, and characterization. *Phys Rev B* **78**, 241103 (2008).
10. Amanti MI, Fischer M, Scalari G et al. Low-divergence single-mode terahertz quantum cascade laser. *Nat Photonics* **3**, 586–590 (2009).
11. Nikitin AY, Guinea F, García-Vidal FJ et al. Edge and waveguide terahertz surface plasmon modes in graphene microribbons. *Phys Rev B* **84**, 161407 (2011).
12. Zhao YC, Wang L, Zhang YX et al. High-speed efficient terahertz modulation based on tunable collective-individual state conversion within an active 3 nm two-dimensional electron gas metasurface. *Nano Lett* **19**, 7588–7597 (2019).
13. Buchnev O, Podoliak N, Kaltenecker K et al. Metasurface-based optical liquid crystal cell as an ultrathin spatial phase modulator for THz applications. *ACS Photonics* **7**, 3199–3206 (2020).
14. Jepsen PU, Cooke DG, Koch M. Terahertz spectroscopy and imaging - modern techniques and applications. *Laser Photonics Rev* **5**, 124–166 (2011).
15. Sensale-Rodriguez B, Yan RS, Kelly MM et al. Broadband graphene terahertz modulators enabled by intraband transitions. *Nat Commun* **3**, 780 (2012).
16. Zhang SJ, Chen XY, Liu K et al. Nonvolatile reconfigurable terahertz wave modulator. *PhotoniX* **3**, 7 (2022).
17. Chen HT, Padilla WJ, Zide JMO et al. Active terahertz metamaterial devices. *Nature* **444**, 597–600 (2006).
18. Yu NF, Genevet P, Kats MA et al. Light propagation with phase discontinuities: generalized laws of reflection and refraction. *Science* **334**, 333–337 (2011).
19. Yu NF, Capasso F. Flat optics with designer metasurfaces. *Nat Mater* **13**, 139–150 (2014).
20. Kildishev AV, Boltasseva A, Shalaev VM. Planar photonics with metasurfaces. *Science* **339**, 1232009 (2013).
21. Yang YM, Wang WY, Moitra P et al. Dielectric meta-reflectarray for broadband linear polarization conversion and optical vortex generation. *Nano Lett* **14**, 1394–1399 (2014).
22. Nemati A, Wang Q, Hong MH et al. Tunable and reconfigurable metasurfaces and metadevices. *Opto-Electron Adv* **1**, 180009 (2018).
23. Peng C , Yao J , Tsai DP . Progress in metalenses: from single to array . *Opto-Electron Technol* **1** , 250004 (2025).
24. Han S, Cong LQ, Srivastava YK et al. All-dielectric active terahertz photonics driven by bound states in the continuum. *Adv Mater* **31**, 1901921 (2019).
25. Yang FY, Tan TC, Prakash S et al. Reconfigurable wide-angle beam-steering terahertz metasurfaces based on vanadium dioxide. *Adv Opt Mater* **12**, 2302047 (2024).
26. Chen BW, Yang SX, Chen J et al. Directional terahertz holography with thermally active Janus metasurface. *Light Sci Appl* **12**, 136 (2023).
27. Venkatesh S, Lu XY, Saeidi H et al. A high-speed programmable and scalable terahertz holographic metasurface based on tiled CMOS chips. *Nat Electron* **3**, 785–793 (2020).
28. Chen BW, Wang XR, Li WL et al. Electrically addressable integrated intelligent terahertz metasurface. *Sci Adv* **8**, eadd1296 (2022).
29. Niu L, Feng X, Zhang XQ et al. Photonic terahertz phased array via selective excitation of nonlinear Pancharatnam-Berry elements. *Nat Commun* **16**, 8159 (2025).
30. Liu M, Plum E, Li H et al. Temperature-controlled optical activity and negative refractive index. *Adv Funct Mater* **31**, 2010249 (2021).
31. Nouman MT, Hwang J, Faiyaz M et al. Dynamic-metasurface-based cavity structures for enhanced absorption and phase modulation. *ACS Photonics* **6**, 374–381 (2019).
32. Liu M, Plum E, Li H et al. Switchable chiral mirrors. *Adv Opt Mater* **8**, 2000247 (2020).
33. Wu PC, Pala RA, Kafaie Shirmanesh G et al. Dynamic beam steering with all-dielectric electro-optic III–V multiple-quantum-well metasurfaces. *Nat Commun* **10**, 3654 (2019).
34. Li JX, Yu P, Zhang S et al. Electrically-controlled digital metasurface device for light projection displays. *Nat Commun* **11**, 3574 (2020).
35. Zhuang XL, Zhang W, Wang KM et al. Active terahertz beam steering based on mechanical deformation of liquid crystal elastomer metasurface. *Light Sci Appl* **12**, 14 (2023).
36. Dong BW, Zhu SQ, Guo GX et al. Switchable Pancharatnam–Berry phases in heterogeneously integrated THz metasurfaces. *Adv Mater* **37**, 2417183 (2025).
37. Guo HB, Chen BW, Li Y et al. Broadband, transmissive, and cascadable terahertz programmable metasurface. *ACS Nano* **19**, 21660–21668 (2025).
38. Guo JY, Wang T, Zhao H et al. Reconfigurable terahertz metasurface pure phase holograms. *Adv Opt Mater* **7**, 1801696 (2019).
39. Yu SL, Xu MF, Pu MB et al. Dynamic nonlocal metasurface for multifunctional integration via phase-change materials. *Nanophotonics* **13**, 4317–4325 (2024).
40. Wang Q, Zhang XQ, Xu YH et al. A broadband metasurface-based terahertz flat-lens array. *Adv Opt Mater* **3**, 779–785 (2015).
41. Zhou YW, Zhang T, Wang GN et al. Directional phase and polarization manipulation using Janus metasurfaces. *Adv Sci* **11**, 2406571 (2024).
42. Nan T, Zhao H, Guo JY et al. Generation of structured light beams with polarization variation along arbitrary spatial trajectories using trilayer metasurfaces. *Opto-Electron Sci* **3**, 230052 (2024).
43. Liu WG, Hu B, Huang ZD et al. Graphene-enabled electrically controlled terahertz meta-lens. *Photonics Res* **6**, 703–708 (2018).
44. Guo YH, Lei YS, Pu MB et al. Vectorial digitelligent optics for high-resolution non-line-of-sight imaging. *Engineering* **45**, 70–78 (2025).
45. Xie X, Pu MB, Jin JJ et al. Generalized Pancharatnam-Berry phase in rotationally symmetric meta-atoms. *Phys Rev Lett* **126**, 183902 (2021).
46. Guo YH, Zhang SC, Pu MB et al. Spin-decoupled metasurface for simultaneous detection of spin and orbital angular momenta via momentum transformation. *Light Sci Appl* **10**, 63 (2021).
47. Pu MB, Li X, Ma XL et al. Catenary optics for achromatic generation of perfect optical angular momentum. *Sci Adv* **1**, e1500396 (2015).
48. Zhao H, Quan BG, Wang XK et al. Demonstration of orbital angular momentum multiplexing and demultiplexing based on a metasurface in the terahertz band. *ACS Photonics* **5**, 1726–1732 (2018).
49. Wang S, Guo HB, Chen BW et al. Electrically active terahertz liquid-crystal metasurface for polarization vortex beam switching. *Laser Photonics Rev* **18**, 2301301 (2024).
50. Zhang Z, Li GY, Liu YL et al. Robust measurement of orbital angular momentum of a partially coherent vortex beam under amplitude and phase perturbations. *Opto-Electron Sci* **3**, 240001 (2024).
51. Zhang L, Liu S, Li LL et al. Spin-controlled multiple pencil beams and vortex beams with different polarizations generated by Pancharatnam-Berry coding metasurfaces. *ACS Appl Mater Interfaces* **9**, 36447–36455 (2017).
52. Li FY, Li YX, Tang TT et al. All-dielectric terahertz metasurface for linearly-polarized multichannel transmission and superposition states of spherical and vortex waves. *Photonics Res* **11**, 485–493 (2023).

53. Li J, Zhang YT, Li JN et al. Amplitude modulation of anomalously reflected terahertz beams using all-optical active Pancharatnam–Berry coding metasurfaces. *Nanoscale* **11**, 5746–5753 (2019).
54. He JW, Wang XK, Hu D et al. Generation and evolution of the terahertz vortex beam. *Opt Express* **21**, 20230–20239 (2013).
55. Chen WT, Yang KY, Wang CM et al. High-efficiency broadband meta-hologram with polarization-controlled dual images. *Nano Lett* **14**, 225–230 (2014).
56. Liu XB, Wang Q, Zhang XQ et al. Thermally dependent dynamic meta-holography using a vanadium dioxide integrated metasurface. *Adv Opt Mater* **7**, 1900175 (2019).
57. Wang Y, Yao ZY, Cui ZJ et al. Orbital angular momentum multiplexing holography based on multiple polarization channel metasurface. *Nanophotonics* **12**, 4339–4349 (2023).
58. Ni XJ, Kildishev AV, Shalaev VM. Metasurface holograms for visible light. *Nat Commun* **4**, 2807 (2013).
59. Goorden SA, Bertolotti J, Mosk AP. Superpixel-based spatial amplitude and phase modulation using a digital micromirror device. *Opt Express* **22**, 17999–18009 (2014).

Acknowledgements

This work was supported by the National Natural Science Foundation of China (12574421, 62275175, 12174270, and 12174271) and Beijing Municipal Natural Science Foundation (2252032).

Author contributions

G. B. Li and Y. Zhang conceived the concept. G. B. Li, G. Y. Li, and H. Ma proposed the device design; G. B. Li performed the numerical simulations; G. Y. Li fabricated the samples; G. B. Li performed the optical measurements with the help of Z. H. He and X. K. Wang; P. J. Klar, H. Ma, and Y. Zhang discussed the results; G. B. Li and G. Y. Li wrote the manuscript; Y. Zhang supervised the project.

Competing interests

Yan Zhang serves as an Editor for the Journal, and no other author has reported any competing interests.

Data availability

The source data is available from the corresponding author upon reasonable request. All data needed to evaluate the conclusion are present in the manuscript and/or the Supplementary Information.

Supplementary information

Supplementary information for this paper is available at
https://doi.org/10.29026/oea.2026.260028

Open Access This article is licensed under a Creative Commons Attribution 4.0 International License, which permits use, sharing, adaptation, distribution and reproduction in any medium or format, as long as you give appropriate credit to the original author(s) and the source, provide a link to the Creative Commons license, and indicate if changes were made. To view a copy of this license, visit http://creativecommons.org/licenses/by/4.0/
©The Author(s) 2026.
Published by Editorial Office of *Opto-Electronic Advance*, Institute of Optics and Electronics, Chinese Academy of Sciences.

Opto-Electronic Journals Group
www.oejournal.org
Scan for Article PDF